COMMUNICATIONS IN SCIENCE AND TECHNOLOGY
Homepage: cst.kipmi.or.id

Analytical modeling of LEO satellite mutual visibility under perturbations

Mohamed R. Amin*

Department of Mathematics, College of Science, Qassim University, Buraydah 51452, Saudi Arabia
Department of Theoretical Physics, National Research Centre, Dokki, Giza 12622, Egypt

Article history:
Received: 13 November 2025 / Received in revised form: 13 December 2025 / Accepted: 17 December 2025

Abstract

This present study develops an analytical model for mutual visibility in perturbed Low Earth Orbit (LEO), explicitly accounting for Earth's oblateness (J_2 and J_3) and atmospheric drag. The framework extends classical geometric visibility calculations to include long-term perturbation effects, thus enabling rapid and reliable prediction of visibility intervals. A series of numerical simulations were conducted on three LEO satellite configurations and revealed that perturbations have the capacity to shift rise–set times, alter event frequency and duration, and generate new visibility intervals. These effects are of particular significance for satellites operating at lower altitudes and those characterized with moderate semi-major axis differences and large inclination disparities. The results of the study underscore the importance of considering secular and long-period perturbations into the planning of reliable communication relay, the management of constellation, and the scheduling of autonomous mission. Importantly, the closed-form formulation enables fast visibility and rise–set prediction without full numerical orbit propagation, supporting preliminary constellation design, inter-satellite link scheduling, and onboard visibility assessment in large LEO networks.

Keywords: Mutual visibility; line of sight; rise and set times; earth's oblateness; atmospheric drag; LEO satellites

1. Introduction

Mutual visibility between satellites in Low Earth Orbit (LEO) is crucial for continuous inter-satellite communication, data relaying, and coordinated mission operations. The rise–set problem determining when two satellites establish or lose a direct line of sight, remains central to the design of crosslink networks, constellation scheduling, and autonomous operations. However, such predictions are significantly influenced by orbital perturbations, particularly Earth's oblateness and atmospheric drag. These effects are particularly significant in long-duration analyses, where even minor deviations in orbital elements can accumulate into substantial shifts in visibility windows. The issue of visibility has been comprehensively addressed in a substantial corpus of literature. In the early stages of analytical research, Escobal [1] provided closed-form formulas to calculate rise–set times around an oblate Earth. Concurrently, Roth [2] examined the factors influencing visibility duration and elevation angle. Lawton [3] subsequently introduced a numerical method adapted for satellites in near-circular orbits, and Alfano et al. [4] extended these calculations by incorporating oblateness corrections. Sun et al. [5] refined Alfano's method and introduced an innovative approach to enhance both efficiency and accuracy. As posited by Han et al. [6], a Hermite interpolation technique was proposed for the expeditious determination of satellite-to-site visibility. Li et al. [8] developed an adaptive interpolation algorithm with vertex protection to achieve more precise and efficient solutions to the satellite visibility period problem. Wang et al. [7] formulated a mathematical model for predicting satellite-to-site and satellite-to-satellite visibility, framing it as a root-finding problem involving multiple hump functions. Awad et al. [9] studied same-orbit visibility functions, while Ammar et al. [10,11] incorporated the effects of drag and oblateness separately. Amin and Hassan [12] further demonstrated the role of lunar perturbations on satellite visibility intervals. Satellite-based systems are increasingly relied upon for Earth observation and positioning, thereby motivating the efficient prediction of mutual-visibility in LEO networks, as discussed in D. Atunggal et al.[13] . Despite these significant contributions, most analytical treatments address perturbations individually rather than in a unified framework. This methodological shortcoming, consequently, limits their accuracy in realistic mission scenarios. In turn, this present study addresses this gap by developing an analytical model for mutual visibility in perturbed LEO orbits. The approach combines classical geometric visibility conditions with perturbative corrections obtained from Lagrange's and Gauss's variational equations. By incorporating secular and long-period effects of Earth's oblateness (J_2, J_3) and atmospheric drag, the model enables closed-form visibility predictions in terms of

* Corresponding author.
Email: m.abdelhameid@qu.edu.sa
https://doi.org/10.21924/cst.10.2.2025.1835

orbital elements and mean anomalies. Numerical case studies involving multiple LEO satellite configurations demonstrate that such perturbations can shift rise–set times, increase event frequency and duration, and even generate new visibility opportunities. In this way, the model provides a practical analytical tool for more reliable mission planning, constellation management, and autonomous scheduling in emerging large-scale LEO networks.

2. Materials and Methods

2.1. Problem formulation

Consider two satellites located in distinct orbits, which are denoted as points S_1 and S_2, respectively. Let ψ denote the angle between the two position vectors $\vec{r}_1$ and $\vec{r}_2$ where $\vec{r}_i = (x_i, y_i, z_i)$, $i = 1,2$. Define the range vector $\vec{\rho}$ as the vector from satellite S_1 to satellite S_2, as geometrically illustrated in Fig. 1.

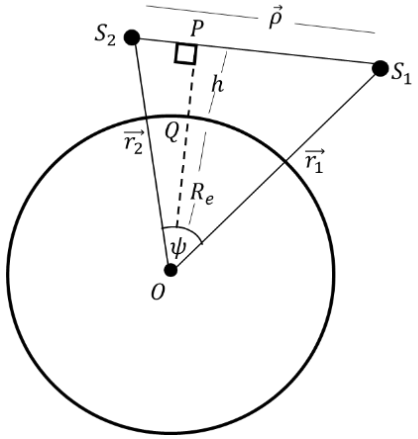

Fig. 1. Geometrical framework of the problem

Let O denote the Earth's center and P a point lying on the position vector ρ. In this context, P is taken as the closest point of the line-of-sight ρ to O. The distance OP is given by $OP = Re + h$, where, R_e is the Earth's mean radius and h is the altitude of point P above the Earth's surface. The satellites are considered mutually visible only when $h > 0$; If $h = 0$ or $h < 0$, the line of sight is obstructed. Formally, the visibility condition is presented as follows:

$$h \begin{cases} > 0 & \text{visibility achieved} \\ = 0 & \text{rise or set case condition} \\ < 0 & \text{visibility not achieved} \end{cases} \quad (1)$$

2.1.1. Visibility function derivation

The geometric relationship between the satellites can be expressed as follows:

$$\vec{r}_1 \cdot \vec{r}_2 - \sqrt{r_1^2 - (R_e + h)^2}\sqrt{r_2^2 - (R_e + h)^2} = (R_e + h)^2 \quad (2)$$

which can be rearranged to:

$$r_1^2\, r_2^2 - (\vec{r}_1 \cdot \vec{r}_2)^2 = (R_e + h)^2\left((r_1{}^2 + r_2{}^2) - 2(\vec{r}_1 \cdot \vec{r}_2)\right) \quad (3)$$

This then leads to:

$$h = \sqrt{\frac{r_1^2\, r_2^2 - (\vec{r}_1 \cdot \vec{r}_2)^2}{(r_1{}^2 + r_2{}^2) - 2(\vec{r}_1 \cdot \vec{r}_2)}} - R_e \quad (4)$$

Visibility between satellites is achieved only if

$$r_1{}^2 r_2{}^2 - (\vec{r}_1 \cdot \vec{r}_2)^2 > R_e^2\left((r_1{}^2 + r_2{}^2) - 2(\vec{r}_1 \cdot \vec{r}_2)\right) \quad (5)$$

Introducing the visibility function V:

$$V = R_e^2\left((r_1{}^2 + r_2{}^2) - 2(\vec{r}_1 \cdot \vec{r}_2)\right) - r_1{}^2 r_2{}^2 + (\vec{r}_1 \cdot \vec{r}_2)^2 \quad (6)$$

the visibility condition can be succinctly expressed as follows:

$$V \begin{cases} < 0 & \text{visibility achieved} \\ 0 & \text{rise or set} \\ > 0 & \text{visibility not achieved} \end{cases} \quad (7)$$

2.1.2. Orbital representation

To express V in terms of the orbital elements, we computed $\vec{r}_1$ and $\vec{r}_2$, using the following expressions for satellite coordinates in an inertial frame [15]

$$\begin{aligned} x &= r(\cos(\Omega)\cos(\omega + f) - \sin(\Omega)\sin(\omega + f)\cos(i)) \\ y &= r(\sin(\Omega)\cos(\omega + f) + \cos(\Omega)\sin(\omega + f)\cos(i)) \\ z &= r\sin(\omega + f)\sin(i) \end{aligned} \quad (8)$$

where f denotes the true anomaly, ω signifies the argument of perigee, Ω represents the right ascension of the ascending node, and i designates the inclination. The rearrangement process then yielded the following results:

$$\begin{aligned} x = {} & r\cos(f)\left(\sin^2\left(\frac{i}{2}\right)\cos(\omega - \Omega) + \cos^2\left(\frac{i}{2}\right)\cos(\omega + \Omega)\right) \\ & - r\sin(f)\left(\sin^2\left(\frac{i}{2}\right)\sin(\omega - \Omega) + \cos^2\left(\frac{i}{2}\right)\sin(\omega + \Omega)\right) \end{aligned} \quad (9a)$$

$$y = r\cos(f)\left(\cos^2\left(\frac{i}{2}\right)\sin(\omega+\Omega) - \sin^2\left(\frac{i}{2}\right)\sin(\omega-\Omega)\right) + r\sin(f)\left(\cos^2\left(\frac{i}{2}\right)\cos(\omega+\Omega) - \sin^2\left(\frac{i}{2}\right)\cos(\omega-\Omega)\right) \tag{9b}$$

$$z = 2\sin\left(\frac{i}{2}\right)\cos\left(\frac{i}{2}\right)(r\sin(f)\cos(\omega) + r\cos(f)\sin(\omega)) \tag{9c}$$

The expression of r, $r\sin f$ and $r\cos f$ as functions of M and expanding to fourth order in in eccentricity e, yielded the following result: [16]

$$r = a\left(\left(1+\frac{1}{2}e^2\right) + \left(-e+\frac{3}{8}e^3\right)\cos(M) + \left(-\frac{1}{2}e^2+\frac{1}{3}e^4\right)\cos(2M) - \frac{3}{8}e^3\cos(3M) - \frac{1}{3}e^4\cos(4M)\right) \tag{10a}$$

$$r\cos(f) = a\left(-\frac{3}{2}e + \left(1-\frac{3}{8}e^2+\frac{5}{192}e^4\right)\cos(M) + \left(\frac{1}{2}e-\frac{1}{3}e^3\right)\cos(2M) + \left(\frac{3}{8}e^2-\frac{45}{128}e^4\right)\cos(3M) + \frac{1}{3}e^3\cos(4M) + \frac{125}{384}e^4\cos(5M)\right) \tag{10b}$$

$$r\sin(f) = a\left(\left(1-\frac{5}{8}e^2-\frac{11}{192}e^4\right)\sin(M) + \left(\frac{1}{2}e-\frac{5}{12}e^3\right)\sin(2M) + \left(\frac{3}{8}e^2-\frac{51}{128}e^4\right)\sin(3M) + \frac{1}{3}e^3\sin(4M) + \frac{125}{384}e^4\sin(5M)\right) \tag{10c}$$

Remark. Although the eccentricities of the configurations considered later were very small (e ≤ 0.01; Table 2), the expansions in Eq. (10) were carried out up to fourth order in e, thereby ensuring the validity of resulting expressions for moderately eccentric LEO orbits. For such small values of *e,* a second–order truncation would already provide excellent accuracy; however, retaining the e^4 terms ensured uniform applicability of the visibility formulation without requiring case–specific rederivations. A numerical examination of the configurations as outlined in Section 3 revealed that truncation of the series at $O(e^2)$ resulted in a change in the predicted rise–set times less than one second. Consequently, the e^4 terms did not influence the conclusions but preserved generality. These expressions facilitate the explicit computation of *x*, *y*, and *z* in terms of orbital elements [12].

$$\begin{aligned} x_j = {} & a_j\left(\sin^2\left(\frac{i_j}{2}\right)\cos(\omega_j-\Omega_j) + \cos^2\left(\frac{i_j}{2}\right)\cos(\omega_j+\Omega_j)\right)\left(-\frac{3}{2}e_j + \left(1-\frac{3}{8}e_j^2+\frac{5}{192}e_j^4\right)\cos(M_j)\right. \\ & \left. + \left(\frac{1}{2}e_j-\frac{1}{3}e_j^3\right)\cos(2M_j) + \left(\frac{3}{8}e_j^2-\frac{45}{128}e_j^4\right)\cos(3M_j) + \frac{1}{3}e_j^3\cos(4M_j) + \frac{125}{384}e_j^4\cos(5M_j)\right) \\ & - a_j\left(\sin^2\left(\frac{i_j}{2}\right)\sin(\omega_j-\Omega_j) + \cos^2\left(\frac{i_j}{2}\right)\sin(\omega_j+\Omega_j)\right)\left(\left(1-\frac{5}{8}e_j^2-\frac{11}{192}e_j^4\right)\sin(M_j)\right. \\ & \left. + \left(\frac{1}{2}e_j-\frac{5}{12}e_j^3\right)\sin(2M_j) + \left(\frac{3}{8}e_j^2-\frac{51}{128}e_j^4\right)\sin(3M_j) + \frac{1}{3}e_j^3\sin(4M_j) + \frac{125}{384}e_j^4\sin(5M_j)\right) \end{aligned} \tag{11}$$

$$\begin{aligned} y_j = {} & a_j\left(\cos^2\left(\frac{i_j}{2}\right)\sin(\omega_j+\Omega_j) - \sin^2\left(\frac{i_j}{2}\right)\sin(\omega_j-\Omega_j)\right)\left(-\frac{3}{2}e_j + \left(1-\frac{3}{8}e_j^2+\frac{5}{192}e_j^4\right)\cos(M_j)\right. \\ & \left. + \left(\frac{1}{2}e_j-\frac{1}{3}e_j^3\right)\cos(2M_j) + \left(\frac{3}{8}e_j^2-\frac{45}{128}e_j^4\right)\cos(3M_j) + \frac{1}{3}e_j^3\cos(4M_j) + \frac{125}{384}e_j^4\cos(5M_j)\right) \\ & + a_j\left(\cos^2\left(\frac{i_j}{2}\right)\cos(\omega_j+\Omega_j) - \sin^2\left(\frac{i_j}{2}\right)\cos(\omega_j-\Omega_j)\right)\left(\left(1-\frac{5}{8}e_j^2-\frac{11}{192}e_j^4\right)\sin(M_j)\right. \\ & \left. + \left(\frac{1}{2}e_j-\frac{5}{12}e_j^3\right)\sin(2M_j) + \left(\frac{3}{8}e_j^2-\frac{51}{128}e_j^4\right)\sin(3M_j) + \frac{1}{3}e_j^3\sin(4M_j) + \frac{125}{384}e_j^4\sin(5M_j)\right) \end{aligned} \tag{12}$$

$$
\begin{aligned}
z_j = 2\sin\left(\frac{i_j}{2}\right)\cos\left(\frac{i_j}{2}\right)\Bigg(a_j\Bigg(&\left(1-\frac{5}{8}e_j^2-\frac{11}{192}e_j^4\right)\sin(M_j)+\left(\frac{1}{2}e_j-\frac{5}{12}e_j^3\right)\sin(2M_j)+\left(\frac{3}{8}e_j^2-\frac{51}{128}e_j^4\right)\sin(3M_j)\\
&+\frac{1}{3}e_j^3\sin(4M_j)+\frac{125}{384}e_j^4\sin(5M_j)\Bigg)\cos(\omega_j)\\
&+a_j\left(-\frac{3}{2}e_j+\left(1-\frac{3}{8}e_j^2+\frac{5}{192}e_j^4\right)\cos(M_j)+\left(\frac{1}{2}e_j-\frac{1}{3}e_j^3\right)\cos(2M_j)\right.\\
&\left.+\left(\frac{3}{8}e_j^2-\frac{45}{128}e_j^4\right)\cos(3M_j)+\frac{1}{3}e_j^3\cos(4M_j)+\frac{125}{384}e_j^4\cos(5M_j)\right)\sin(\omega_j)\Bigg)
\end{aligned}
\tag{13}
$$

Thus, the dot product is:

$$(\vec{r}_1\cdot\vec{r}_2)=x_1x_2+y_1y_2+z_1z_2 \tag{14}$$

The squared radii, expanded up to fourth order in e, are expressed as follows:

$$
\begin{aligned}
r_j^2 = a_j^2\Bigg(&\left(1+\frac{3}{2}e_j^2\right)-2e_j\left(1-\frac{1}{8}e_j^2\right)\cos(M_j)\\
&-\frac{1}{2}e_j\left(1-\frac{1}{3}e_j^2\right)\cos(2M_j)\\
&-\frac{1}{4}e_j^3\cos(3M_j)-\frac{1}{6}e_j^4\cos(4M_j)\Bigg)
\end{aligned}
\tag{15}
$$

Consequently, visibility function V can be expressed entirely in terms of the orbital elements and mean anomalies. This facilitates accurate evaluation of mutual satellite visibility in orbit.

2.2. *Perturbation modeling of orbital elements*

The evolution of satellite orbits in LEO is influenced by several perturbative forces, the most significant of which are Earth's oblateness and atmospheric drag. This section formulates the corresponding variations in the orbital elements and incorporates these effects into the visibility function.

2.2.1. Earth's oblateness

Earth is modeled as an axially symmetric body, whose gravitational potential for satellite motion is described by an expansion in zonal harmonics. In this work, the disturbing potential incorporates terms up to J_3, [14.]. This equation can be expressed as follows:

$$\Re=-\frac{\mu}{r}\left(J_2\left(\frac{R_e}{r}\right)^2P_2(\sin\varphi)+J_3\left(\frac{R_e}{r}\right)^3P_3(\sin\varphi)\right) \tag{16}$$

In this equation, μ represents the standard gravitational parameter, R_e denotes the Earth's radius, and P_2, P_3 denote the second and third Legendre polynomials, respectively. This present study focuses on the effects caused by terms that contain secular and long-period contributions only. Therefore, the mean anomaly M was employed as the fast variable to calculate the average of disturbing potential over a short period.

$$\langle\Re\rangle=\frac{1}{2\pi}\int_0^{2\pi}R_m\,dM$$

The averaged disturbing potential was divided into two parts: a secular part and a long-period part,

$$\langle\Re\rangle=\Re_{sec}+\Re_{lp} \tag{17}$$

The subscripts "*sec*" and "*lp*" stand for secular and long-period, respectively, where

$$\Re_{sec}=\frac{1}{4}\mu J_2\frac{R_e^2}{a^3}\frac{(2-3\sin^2 i)}{(1-e^2)^{\frac{3}{2}}} \tag{18}$$

$$\Re_{lp}=\frac{3}{8}\mu J_3\frac{R_e^3}{a^4}\frac{e(4-5\sin^2 i)}{(1-e^2)^{\frac{5}{2}}}\sin i\sin\omega \tag{19}$$

To represent the variation of the orbital elements due to oblateness, in this present study, the Lagrange planetary equations [17] were employed. Denoting the orbital elements by

$$
\begin{aligned}
\frac{da}{dt}&=\frac{2}{n\,a}\frac{\partial\bar{\Re}}{\partial M}\\
\frac{de}{dt}&=-\frac{1-e^2}{na^2e}\left(\frac{1}{\sqrt{1-e^2}}\frac{\partial\bar{\Re}}{\partial\omega}-\frac{\partial\bar{\Re}}{\partial M}\right)\\
\frac{di}{dt}&=\frac{1}{na^2\sqrt{1-e^2}\ \sin i}\left(\cos i\frac{\partial\bar{\Re}}{\partial\omega}-\frac{\partial\bar{\Re}}{\partial\Omega}\right)\\
\frac{d\Omega}{dt}&=\frac{1}{na^2\sqrt{1-e^2}\sin i}\left(\frac{\partial\bar{\Re}}{\partial i}\right)\\
\frac{d\omega}{dt}&=\frac{1}{na^2\sqrt{1-e^2}}\left(\frac{1-e^2}{e}\frac{\partial\bar{\Re}}{\partial e}-\frac{\cos i}{\sin i}\frac{\partial\bar{\Re}}{\partial i}\right)\\
\frac{dM}{dt}&=n-\frac{1}{na^2}\left(\frac{1-e^2}{e}\frac{\partial\bar{\Re}}{\partial e}+2a\frac{\partial\bar{\Re}}{\partial a}\right)
\end{aligned}
\tag{20}
$$

From Eq. (18), (19), and (20), the variations of orbital elements due to oblateness are

$$\Delta_1 a = 0$$

$$\Delta_1 e = -\frac{1}{2}\left(\frac{R_e}{a}\right)\frac{J_3}{J_2}\sin i \sin\omega$$

$$\Delta_1 i = \frac{1}{2}\left(\frac{R_e}{a}\right)\frac{J_3}{J_2}\frac{e}{(1-e^2)}\cos i \sin\omega$$

$$\Delta_1 \omega = \frac{3}{4}\left(\frac{R_e}{a}\right)^2 J_2 \frac{(4-5\sin^2 i)}{(1-e^2)^2} n\,(t-t_0) - \frac{1}{16}\left(\frac{R_e}{a}\right)\frac{J_3}{J_2}\frac{(1+3e^2+4\,cos\,2\,i-5(1+7e^2)\,cos\,4\,i)\,csc\,i}{e(1-e^2)(4-5\,sin^2\,i)}\cos\omega \tag{21}$$

$$\Delta_1 \Omega = -\frac{3}{2}\left(\frac{R_e}{a}\right)^2 J_2 \frac{\cos i}{(1-e^2)^2} n\,(t-t_0) - \frac{1}{8}\left(\frac{R_e}{a}\right)\frac{J_3}{J_2}\frac{e(\cos i + 15\cos 3i)\csc i}{(1-e^2)(4-5\sin^2 i)}\cos\omega$$

$$\Delta_1 M = \left(1+\frac{3}{4}\left(\frac{R_e}{a}\right)^2 J_2 \frac{(2-3\sin^2 i)}{(1-e^2)^{\frac{3}{2}}}\right) n\,(t-t_0) + \frac{1}{2}\left(\frac{R_e}{a}\right)\frac{J_3}{J_2}\frac{(1-4e^2)}{e(1-e^2)^{\frac{1}{2}}}\sin i \cos\omega$$

For the low-Earth orbits under consideration, the secular contribution of the J_2 term dominates the long-term evolution of Ω and ω, thereby generating most of the systematic timing shifts that occur within the mutual-visibility windows. By contrast, the J_3 component primarily induces long-period oscillations in ω and e about their J_2-driven trends. These appear in the visibility function as modest modulations of hump amplitudes and shapes rather than as large, uniform offsets in rise–set times. This separation of roles is employed in Section 3 when interpreting numerical examples. The resulting expressions provide a comprehensive representation of the secular and long-period variations of the orbital elements caused by Earth's oblateness.

2.2.2. Atmospheric drag

The aerodynamic drag force acting on a satellite of mass m, reference area A, and drag coefficient C_D is expressed as [18]

$$F_D = -\frac{1}{2}\rho(h) C_D \frac{A}{m} v_{rel}^2\, \hat{\mathbf{v}}_{rel}, \tag{22}$$

where $\rho(h)$ denotes the atmospheric density at altitude h, v_{rel} refers to the relative velocity between the satellite and the rotating atmosphere, and $\hat{\mathbf{v}}_{rel}$ indicates its unit vector. For a Keplerian orbit, the orbital speed is constrained by the vis-viva relation $v_{rel}^2 = \mu\left(\frac{2}{r}-\frac{1}{a}\right)$, which is used to express the drag acceleration in terms of r and a. The density profile is modeled by an exponential function, with the scale height as H.

$$\rho(h) = \rho_0 \exp\left(-\frac{h-h_0}{H}\right),$$

The representative order-of-magnitude ranges of ρ(h) over typical very-low-LEO to LEO altitudes (100–500 km) are summarized in Table 1.

Table 1. Representative atmospheric density ranges versus altitude (100–500 km)

Altitude (km)	Atmospheric Density (kg·m^{-3})
100	4.97×10^{-7}
150	$(1.13 – 1.25) \times 10^{-8}$
200	$(2.55 – 3.16) \times 10^{-10}$
250	$(0.658 – 1.05) \times 10^{-10}$
300	$(1.7 – 3.5) \times 10^{-11}$
350	$(0.612 – 1.62) \times 10^{-11}$
400	$(2.2 – 7.5) \times 10^{-12}$
450	$(0.938 – 3.87) \times 10^{-12}$
500	$(0.4 – 2.0) \times 10^{-12}$

where ρ_0 denotes the density at the reference altitude h_0. Since aerodynamic drag opposes the satellite's motion, the drag acceleration acts predominantly along the transverse (tangential) direction of the orbital frame. Therefore, in the radial–transverse–normal (*R, T, N*) frame, the perturbing acceleration has components:

$$\boldsymbol{a_d} = (R,\ \ T,\ \ N) \approx (0,\ \ T,\ \ 0)$$

where T is the transverse component corresponding to drag.

$$T = -\frac{\mu}{2}\rho(h)\, C_d \frac{A}{m}\left(\frac{2}{r}-\frac{1}{a}\right)$$

Gauss's variational equations for the osculating elements (*a, e, i, Ω, ω, M*) under a generic perturbation (R, T, N) are well known:[17]

$$\frac{da}{dt} = \frac{2}{n\sqrt{1-e^2}}[e\,R\sin f\ + T(1+e\cos f\,)],$$
$$\frac{de}{dt} = \frac{\sqrt{1-e^2}}{na}\left[R\sin f + T\left(\cos f + \frac{e+\cos f}{1+e\cos f}\right)\right], \qquad (24)$$
$$\frac{di}{dt} = \frac{r\cos(\omega+f)}{na^2\sqrt{1-e^2}}N,$$
$$\frac{d\Omega}{dt} = \frac{r\sin(\omega+f)}{na^2\sqrt{1-e^2}\sin i}N,$$
$$\frac{d\omega}{dt} = \frac{\sqrt{1-e^2}}{nae}\left[-R\cos f\ + T\left(\frac{2+e\cos f}{1+e\cos f}\right)\right] - \cos i\frac{d\Omega}{dt},$$
$$\frac{dM}{dt} = n - \frac{2r}{na}R - \frac{\sqrt{1-e^2}}{nae}\left[-\cos f\ R + \left(\frac{2+e\cos f}{1+e\cos f}\right)T\right],$$

Substituting the drag-dominated acceleration and averaging over one orbital period, and expanding in powers of e up to fourth order results in the time rates of change of the orbital elements due to drag,

$$\Delta_2 a = -na^2\rho C_d\,\frac{A}{m}\left(1+\frac{3}{4}e^2+\frac{21}{64}e^4\right)(t-t_0),$$
$$\Delta_2 e = -na\rho C_d\,\frac{A}{m}\left(\frac{1}{2}e-\frac{5}{16}e^3\right)(t-t_0),$$
$$\Delta_2 i = \Delta_2\omega = \Delta_2\Omega = \Delta_2 M = 0.$$

At first glance, the mean anomaly appears unperturbed; however, this observation is incomplete due to the indirect effect of drag-induced secular changes in the semi-major axis and eccentricity indirectly on the mean anomaly. The relation is expressed as follows:

$$\frac{dM}{dt} = n - \frac{3}{2}\frac{n}{a}\frac{da}{dt} + \frac{1-e^2}{e}\frac{de}{dt}$$

Thus, any alteration in a and e necessarily introduces a corresponding variation in *M*. Even though the averaged Gauss equations for *M* demonstrate zero direct effect from drag, its influence manifests indirectly through the coupled secular changes in the semi-major axis and eccentricity. This behavior is fully consistent with classical atmospheric-drag theory, in which the secular decay of a under drag leads to a corresponding secular change in mean motion and hence in the mean anomaly. In the low-Earth-orbit regime, the dynamic significance of atmospheric drag is strongly altitude dependent. For orbital altitudes of order a few hundred kilometers, standard exponential-density models predict secular decay of the semi-major axis on time scales comparable with typical mission durations. Consequently, drag-induced variations in the mean motion and orbital phase cannot be neglected when analyzing mutual visibility. The example configurations considered later fall within this regime and drag therefore acts as a genuinely coupled perturbation alongside the J_2 and J_3 effects.

$$\Delta_2 a = -na^2\rho C_d\,\frac{A}{m}\left(1+\frac{3}{4}e^2+\frac{21}{64}e^4\right)(t-t_0),$$
$$\Delta_2 e = -na\rho C_d\,\frac{A}{m}\left(\frac{1}{2}e-\frac{5}{16}e^3\right)(t-t_0), \qquad (25)$$
$$\Delta_2 i = \Delta_2\omega = \Delta_2\Omega = 0$$
$$\Delta_2 M = n(t-t_0) - \frac{3}{2}\frac{1}{a}\Delta_2 a + \frac{1-e^2}{e}\Delta_2 e.$$

2.2.3. Perturbed visibility function

The perturbed visibility function *F* is then expressed as:

$$F(a_j, e_j, i_j, \Omega_j, \omega_j, M_j) = V(a_{j0}, e_{j0}, i_{j0}, \Omega_{j0}, \omega_{j0}, M_{j0}) + \sum_{i=1}^{12}\left(\frac{\partial V}{\partial \alpha_i}\right)(\Delta_1\alpha_i + \Delta_2\alpha_i) \qquad (26)$$

where $V(a_{j0}, e_{j0}, i_{j0}, \Omega_{j0}, \omega_{j0}, M_{j0})$ is the unperturbed visibility function. The elements α_i represent the orbital elements of the satellites: for $i = 1, \ldots, 6$, α_i correspond to $a, e, i, \omega, \Omega, M$ of the first satellite; for $i = 7, \ldots, 12$, they correspond to $a, e, i, \omega, \Omega, M$ of the second satellite.

3. Results and Discussion

The perturbed visibility function F was applied to case studies to evaluate the mutual visibility of satellites at varying altitudes. The orbital parameters are summarized in Table 2 in which the semi-major axes are geocentric, corresponding to approximate orbital altitudes of approximately 150 km, 320 km, and 460 km for Satellites #1–#3, respectively. Although 150 km is at the very low end of LEO and typically not sustained for long, it is included here as a very-low-LEO stress-test scenario to demonstrate the coupled J_2–J_3–drag impact on mutual-visibility timing over a 24-hour horizon. At 150–320 km, the adopted exponential-density model implies non-negligible drag over a 24-hour window, consistent with the few-minute visibility shifts reported below. The influence of perturbative effects, specifically Earth's oblateness and atmospheric drag, was systematically examined. These effects are illustrated in Figs. 2–4, which present a comparison of the visibility function, evaluated with and without perturbations, over a 24-hour period. The associated rise and set times are documented in Tables 3–5, providing comprehensive quantification of the visibility intervals.

Table 2 Orbital Parameters of LEO Satellites at Various Altitudes

	Orbital Parameters						
	a (Km)	e	i (°)	Ω (°)	ω (°)	M (°)	n ($^{rad/min}$)
Satellite #1	6525.17	0.0082	96.71	214.85	281.05	206.35	7.18×10^{-2}
Satellite #2	6700.49	0.0096	19.96	299.53	286.90	72.07	6.93×10^{-2}
Satellite #3	6841.56	0.0011	51.64	249.97	3.90	356.21	6.70×10^{-2}

3.1. Satellites #1 and #2

Fig. 2 illustrates the visibility function for Satellites #1 and #2 over a 24-hour period, with a comparison of the perturbed and unperturbed cases. The satellites' orbital configuration, with a moderate difference in semi-major axis (a1 = 6525.17 km vs. a2 = 6700.49 km, corresponding to altitudes of about 150 km and 320 km above the mean Earth radius) and a significant inclination disparity (96.71 deg vs. 19.96 deg), results in pronounced sensitivity to Earth's oblateness and atmospheric drag. The perturbed visibility function demonstrates systematic shifts in rise–set times (up to approximately 3 minutes, or about 2% of the orbital period) and amplitude enhancements, particularly after 600 minutes, reflecting long-period perturbation effects. Table 3 quantifies these impacts, demonstrating that perturbations increase the frequency of visibility events and extend durations by up to approximately 20%. These findings highlight the critical role of perturbative corrections in the optimization of communication windows for LEO satellites exhibiting disparate orbital parameters. For this pair, the predominant effect is the differential J2-driven precession of the ascending nodes, which gradually rotates the orbital planes relative to one another and accounts for the nearly monotonic shift of rise–set times over the 24-hour interval. Long-period variations in the argument of perigee and eccentricity, driven primarily by J3, manifest as modest changes in the peak amplitudes of the visibility humps. At the lower altitude of Satellite #1, atmospheric drag further reduces the semi-major axis and mean motion, thereby introducing an additional relative phasing that contributes to the short extra visibility windows that appear in the perturbed case.

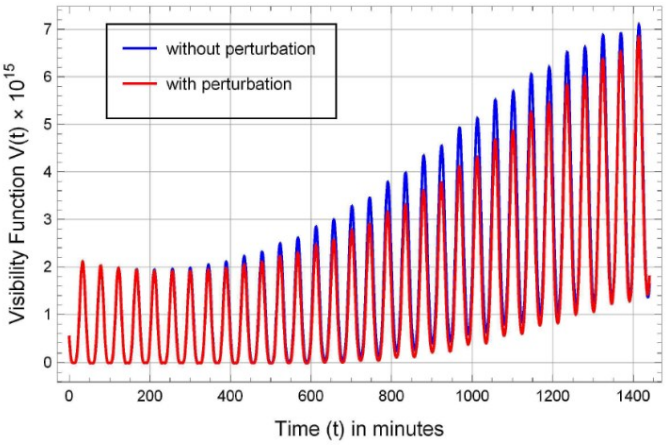

Fig. 2 Visibility Function for Satellites #1 and #2 over 24 Hours: Perturbed vs. Unperturbed Cases

Table 3. 24-hour visibility intervals between Satellites #1 and #2

Unperturbed Case				Perturbed Case			
Rise (min)	Set (min)	Time of Visibility		Rise (min)	Set (min)	Time of Visibility	
		min	Sec			min	sec
7.8379	14.2886	6	27.05	7.7930	14.3055	6	30.75
50.5521	60.6106	10	3.51	50.6146	60.4993	9	53.08
95.9310	104.3115	8	22.83	95.9163	104.2271	8	18.65
139.0937	150.1350	11	2.48	139.1115	150.0023	10	53.45
184.6276	188.2224	3	35.69	184.5124	188.2407	3	43.70
189.8768	193.7252	3	50.90	189.7251	193.6623	3	56.23
228.0516	232.7587	4	42.42	227.9269	232.5136	4	35.20
234.7991	239.2399	4	26.45	234.8059	239.1677	4	21.71
273.8110	282.6497	8	50.32	273.4555	277.4266	3	58.27
				278.6139	282.7168	4	6.17
317.4184	327.9383	10	31.19	317.0258	322.3604	5	20.08
				322.9902	328.0219	5	1.90
363.5178	371.0519	7	32.05	362.6998	371.4253	8	43.53
407.2527	416.1766	8	55.44	406.3970	416.5733	10	10.58
454.0720	458.6110	4	32.34	452.2752	459.7684	7	29.59
497.8130	503.7002	5	52.34	496.0774	504.7931	8	42.94
-	-	-	-	542.3922	547.5598	5	10.06
-	-	-	-	586.2426	592.5206	6	16.68

3.2. Satellites #1 and #3

Fig. 3 illustrates the visibility function for Satellites #1 and #3 over a 24-hour period, with a comparison of the perturbed and unperturbed cases. The satellites' orbital configuration, characterized by a significant disparity in semi-major axis (6525.17 km vs. 6841.56 km, i.e., altitudes of approximately 150 km and 460 km) and an intermediate inclination for Satellite #3 (51.64 deg, between 96.71 deg for Satellite #1 and 19.96 deg for Satellite #2), results in moderate sensitivity to Earth's oblateness and atmospheric drag. In this configuration, the greater separation in semi-major axis makes the geometry particularly sensitive to differential nodal precession. The secular J2-driven drift in Ω produces the primary timing offsets between the perturbed and unperturbed curves, while the weaker J3-induced modulation of ω and e primarily affects the fine structure of the visibility humps. As in the previous case, the drag in the lower orbit modifies the mean motion of Satellite #1, thereby enhancing the relative phasing and helping to bring near-threshold humps above the visibility limit. This explains the appearance of additional short windows in the perturbed solution. The perturbed visibility function demonstrates shifts in rise–set times (up to approximately 2 minutes, or about 1.5% of the orbital period) and introduces new visibility intervals, with duration changes of up to about 15%. Table 4 quantifies these effects, indicating that perturbations exhibit a reduced impact in comparison to the Satellite #1–#2 pair due to Satellite #3's higher altitude, which mitigates drag effects. Visibility peaks remain largely synchronized, with discrepancies primarily manifesting as minor shifts and extensions after 300 minutes.

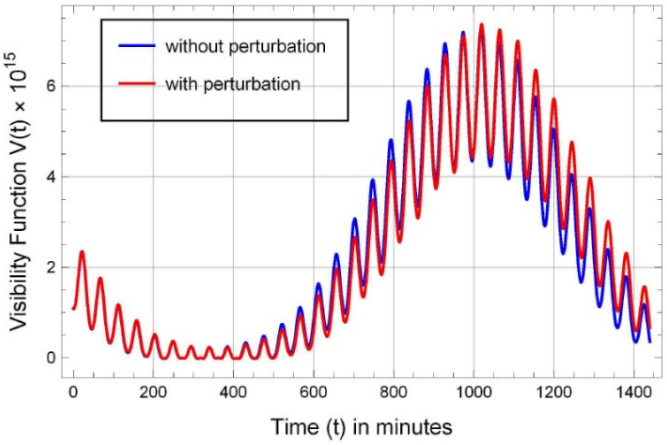

Fig. 3 Visibility Function for Satellites #1 and #3 over 24 Hours: Perturbed vs. Unperturbed Cases

Table 4 24-hour visibility intervals between Satellites #1 and #3.

Unperturbed Case				Perturbed Case			
Rise (min)	Set (min)	Time of Visibility		Rise (min)	Set (min)	Time of Visibility	
		min	sec			min	sec
220.8656	232.1233	11	15.46	221.7638	231.6132	9	50.96
264.6407	279.5003	14	51.58	265.0220	279.4767	14	27.28
306.8816	315.9952	9	6.82	307.3530	326.6765	19	19.41
317.9478	326.4656	8	31.07				
353.2755	359.3434	6	4.07	353.2802	359.3114	6	1.87
364.1262	371.0510	6	55.49	364.8746	371.7684	6	53.63
398.0189	415.5477	17	31.73	397.9862	416.5846	18	35.90
447.76188	456.8319	9	4.20	446.5640	459.1042	12	32.41
-	-	-	-	494.8345	500.8287	5	59.65

3.3. Satellites #2 and #3

Fig. 4 illustrates the visibility function for Satellites #2 and #3 over a 24-hour period, with a comparison of the perturbed and unperturbed cases. The satellites' orbital configuration, with elevated semi-major axes (6700.49 km and 6841.56 km, corresponding to altitudes of approximately 320 km and 460 km) and disparate inclinations (19.96 deg vs. 51.64 deg), results in moderate sensitivity to Earth's oblateness and atmospheric drag. The perturbed visibility function exhibits systematic shifts in rise-set times (up to approximately 2.5 minutes, or about 1.8% of the orbital period) and introduces new visibility intervals, with duration changes of up to about 25%. Table 5 quantifies these effects, demonstrating an increase in visibility event frequency and redistribution of observation windows. Because both satellites in this pair operate at higher altitudes, drag effects are weaker and the visibility shifts are dominated by J_2-driven nodal precession and perigee rotation. The resulting perturbations generate smaller but still noticeable offsets in rise–set times and a redistribution of visibility intervals, with J_3-induced variations in ω and e again appearing mainly as changes in the amplitudes and shapes of individual humps. The additional windows, as documented in Table 5, are therefore a consequence of the similar cumulative phasing mechanism as in the lower-altitude cases, but with reduced drag sensitivity. These results highlight the pivotal role of perturbative corrections in optimizing mission planning for LEO satellites at higher altitudes with varying orbital geometries.

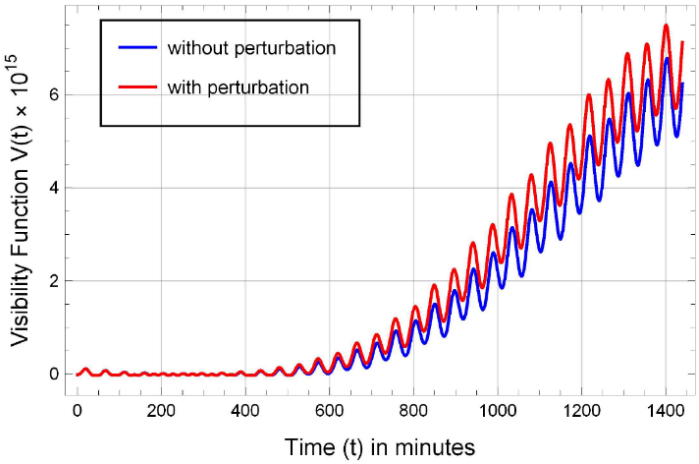

Fig. 4 Visibility Function for Satellites #2 and #3 over 24 Hours: Perturbed vs. Unperturbed Cases

Table 5 24-hour visibility intervals between Satellites #2 and #3

Unperturbed Case				Perturbed Case			
Rise (min)	Set (min)	Time of Visibility		Rise (min)	Set (min)	Time of Visibility	
		min	sec			min	sec
31.8321	56.1497	24	19.06	31.7771	56.2890	24	30.72
77.7241	103.1940	25	28.20	77.1395	103.3892	26	14.98
119.6014	152.7050	33	6.21	119.1355	153.0336	33	53.89
165.9313	199.1244	33	11.58	164.8985	199.1870	34	17.31
208.7258	247.2256	38	29.98	208.0718	226.7556	18	41.03
				228.2514	247.3305	19	4.75
256.1718	272.2631	16	5.48	255.1199	272.0968	16	58.61
275.5172	291.7333	16	12.97	274.6143	290.9878	16	22.41
300.9136	338.1489	37	14.12	300.8132	337.2859	36	28.36
350.1366	380.9469	30	48.61	349.9237	379.5137	29	35.40
396.4124	426.8320	30	25.17	396.8765	425.2733	28	23.81
446.7445	468.5233	21	46.73	447.4127	466.3976	18	59.10
493.5909	514.1568	20	33.95	494.8999	511.7054	16	48.33
548.2879	551.4034	3	6.93	-	-	-	-

This present paper has developed an analytical framework for predicting mutual visibility between low-Earth-orbit satellites under the combined effects of Earth's oblateness and atmospheric drag. The model starts from a perturbed two-body description, incorporating the secular J2 contribution, the long-period J3 effects, and drag-induced decay of the semi-major axis and eccentricity. These perturbations are then propagated into a closed-form visibility function F(t) for a given satellite pair. The formulation was applied to three representative LEO configurations, spanning altitudes of approximately 150 km, 320 km, and 460 km and differing inclinations. For each pair, we compared the unperturbed and perturbed visibility functions over a 24-hour interval. The numerical results presented in Fig. 2–4 and Tables 3–5 conclude that even minimal perturbations can induce non-negligible alteration in mutual visibility in both rise and set times, and the emergence of additional brief visibility windows in the perturbed solutions, particularly when one satellite operates at very low altitude. From dynamic and geometrical perspective, the visibility function can be viewed as a multi-hump function of time, each of which corresponds to a potential line-of-sight opportunity as the two orbits re-phase. The secular J2 term dominates the long-term evolution of Ω and ω, thereby generating most of the systematic timing offsets observed in the visibility windows. Whereas, J3 primarily induces long-period oscillations in ω and e that manifest as modest changes in the amplitudes and shapes of the humps. Atmospheric drag modifies the semi-major axis and mean motion, particularly at the lowest altitudes, thereby introducing an additional phase drift between the satellites. When an unperturbed hump is located close to the visibility threshold, these combined perturbations can shift its maximum above or below the threshold. This process can result in the creation or suppression of short visibility intervals. The additional windows reported in Tables 3–5 arise from this mechanism and are therefore a geometric consequence of small but cumulative perturbations rather than numerical artefacts. In practical terms, the proposed framework provides a rapid tool for estimating mutual visibility and rise-set times without the need for full numerical propagation. This makes it suitable for preliminary design and trade-off studies in LEO constellations, including relay placement and inter-satellite link scheduling. The present analysis focuses on the dominant secular and long-period effects of J2, J3, and drag over a one-day horizon in low Earth orbit. Short-period J2 terms, solar radiation pressure, and third-

body perturbations are neglected and it is expected that they will contribute at most at the percent level for the regimes considered. Accordingly, the present manuscript focuses on the dominant secular and long-period drivers over the one-day horizon, while these smaller effects are left for a straightforward extension of the same analytical structure. Future work will extend the framework to include these additional perturbations, explore longer time spans, and generalize the methodology to multi-satellite constellations with more complex field-of-view constraints.

Data Availability

No new data was generated or analyzed in this study.

Funding

This research did not receive any specific grant from funding agencies in the public, commercial, or non-profit sectors.

References

1. P.R. Escobal, Rise and set times of a satellite about an oblate planet, AIAA J. 1(10) (1963) 2306-2310.
2. E.A. Roth, Rise-and-set time and maximum elevation of a satellite, ESA Sci. Tech. Rev. 2(1) (1976) 620-623.
3. J.A. Lawton, Numerical method for rapid determining satellite–satellite and satellite–ground station in-view periods, J. Guid. Control Dyn. 10(1) (1987) 32-36.
4. S. Alfano, D. Negron Jr., J.L. Moore, Rapid determination of satellite visibility periods, J. Astronaut. Sci. 40(2) (1992) 281-296.
5. X.C. Sun, H.Z. Cui, C. Han, APCHI technique for rapidly and accurately predicting multi-restriction satellite visibility, Proc. 22nd AAS/AIAA Space Flight Mech. Meet. (2012) 212-216.
6. C. Han, X.J. Gao, X.C. Sun, Rapid satellite-to-site visibility determination based on self-adaptive interpolation technique, Sci. China Technol. Sci. 60 (2017) 264-270.
7. X. Wang, L. Liu, G. Tang, Onboard satellite visibility prediction using metamodeling based framework, Aerosp. Sci. Technol. 94 (2019) 105377.
8. X. Li, X. Wang, G. Tang, Fast determination of satellite-to-moon visibility using an adaptive interpolation method based on vertex protection, Sensors 22(12) (2022) 4451.
9. M.E. Awad, M.A. Sharaf, E.H. Khatab, Visual contact between two Earth's satellites, Am. J. Appl. Sci. 9 (2012) 620-623.
10. M.K. Ammar, M.R. Amin, M.H.M. Hassan, Calculation of line of sight periods between two artificial satellites under the action of air drag, Appl. Math. Nonlinear Sci. 3 (2018) 339-352.
11. M.K. Ammar, M.R. Amin, M.H.M. Hassan, Visibility intervals between two artificial satellites under the action of Earth oblateness, Appl. Math. Nonlinear Sci. 3 (2018) 353-374.
12. M.R. Amin, M.H.M. Hassan, Influence of lunar perturbation as a third-body perturbation on satellite visibility intervals, Partial Differ. Equ. Appl. Math. 11 (2024) 100771.
13. D. Atunggal, N. Widjajanti, T. Aditya, Evaluating 3-D positioning infrastructure quality and utilization: The potential improvement with multi-GNSS methods, Commun. Sci. Technol. 9 (2024) 144-152.
14. L. Liu, Algorithms for Satellite Orbital Dynamics, Springer, Singapore, 2023.
15. M. Capderou, Satellites: Orbits and Missions, Springer-Verlag, Paris, 2005.
16. D. Brouwer, G.M. Clemence, Methods of Celestial Mechanics, Academic Press, New York, 1961.
17. G. Xu, Orbits, Springer, Berlin, Heidelberg, 2008.
18. A.E. Roy, Orbital Motion, 4th ed., IOP Publishing, Bristol, U.K., 2005.